Modeling iron-catecholates binding to NGAL protein

Cristina Gómez-Casado , Franziska Roth-Walter , Erika Jensen-Jarolim ,
Araceli Díaz-Perales , Luis F. Pacios

Keywords:
Iron chelators
Catechols
Lipocalins
Electrostatic potential
Protein–ligand docking
Protein–ligand interfaces

A B S T R A C T

Neutrophil gelatinase associated lipocalin (NGAL) protein is attracting a great interest because of its antibacterial properties played upon modulating iron content in competition against iron acquisition processes developed by pathogenic bacteria that bind selective ferric iron chelators (siderophores). Besides its known high affinity to enterobactin, the most important siderophore, it has been recently shown that NGAL is able to bind Fe(III) coordinated by catechols. The selective binding of Fe(III)-catechol ligands to NGAL is here studied by using iron coordination structures with one, two, and three catecholate ligands. By means of a computational approach that consists of B3LYP/6-311G(d,p) quantum calculations for geometries, electron properties and electrostatic potentials of ligands, protein–ligand flexible docking calculations, analyses of protein–ligand interfaces, and Poisson–Boltzmann electrostatic potentials for proteins, we study the binding of iron catecholate ligands to NGAL as a central member of the lipocalin family of proteins. This approach provides a modeling basis for exploring *in silico* the selective binding of iron catecholates ligands giving a detailed picture of their interactions in terms of electrostatic effects and a network of hydrogen bonds in the protein binding pocket.

1. Introduction

Lipocalins are small, secreted proteins important in defense against diseases that act as carriers of hydrophobic molecules and share a characteristic structural feature called "lipocalin fold" [1,2] that consists of an antiparallel β barrel structure made of eight β sheets arranged in an antiparallel orientation resulting in a cup-shaped cavity (the "calyx") that binds, transports, and delivers small ligands [3]. About ten lipocalins are abundant in the human body but one in particular is attracting a considerable interest: neutrophil gelatinase associated lipocalin (NGAL), also known as lipocalin 2 (Lcn2) or 24p3 protein. Recent reports have shown that NGAL is a promising diagnostic and prognostic biomarker in numerous diseases including inflammation and cancer [4]. An engineered NGAL has been shown to offer potential for immunotherapy of cancer and infectious disease [5].

NGAL has also been proposed as an antibacterial component that acts by modulating iron content [6]. About 75% of iron in the average human body participates in oxygen transport in hemoglobin, another 15% is involved in other cellular functions and the remaining portion is bound by transport and storage proteins [7]. With nearly all the iron trapped inside proteins, the concentration of free iron (in the form of Fe^{3+} ion) is estimated at 10^{-24} M [8]. Since pathogenic bacteria must compete against this exceedingly low limit, they have evolved aggressive iron acquisition processes to produce and secrete selective iron chelators called siderophores (from the Greek, meaning "iron carriers"). Siderophores are Fe(III)-specific chelating agents with an affinity for iron several times higher than that of the endogenous iron chelators which enable them to not only bind available free Fe(III), but also extract it from iron-binding proteins of the host [4]. *Escherichia coli* enterobactin, a catecholate type chelator, is the prototype of bacterial siderophores and the best understood of siderophore-mediated iron uptake systems [8]. NGAL exerts its bacteriostatic effect by binding to bacterial siderophores as this lipocalin is released from the liver and spleen in response to an acute bacterial infection [4]. This has raised the question of whether siderophore-like proteins do exist in mammals that could interact with NGAL [4,7]. In 2010, a report had provided

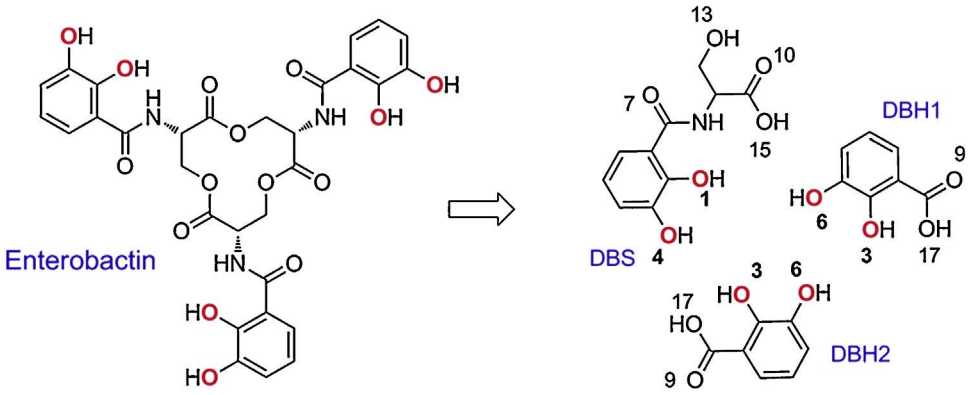

Fig. 1. Enterobactin siderophore is represented by the DBS–DBH1–DBH2 aggregate in the X-ray structure of its complex with wild type NGAL protein (PDB code 1L6M). Iron-binding O atoms are shown in red. Atom numbering refers to the X-ray structure.

an answer to this question showing that NGAL binds iron together with catechols occurring as metabolites [9].

Fe(III)-catecholate ligands have shown significant affinity for NGAL. As catechols are formed in bacterial and mammalian metabolism from polyphenols and aromatic amino acids [10], the formation of the NGAL-catechol-Fe(III) complex blocks the reactivity of iron permitting its transport *in vivo*[9]. Enterobactin is found to inhibit the binding of catechol to NGAL, supporting the idea that bacterial siderophores compete with endogenous siderophore-like compounds to bind free iron. The interaction of NGAL with both enterobactin-Fe(III) and catechol-Fe(III) occurs in the calyx where two basic amino acids (K125 and K134) are instrumental in binding ligands [9]. Binding of catechol-Fe(III) is experimentally described by two dissociation constants, which suggests a stepwise addition. In fact, it has been proposed that the recruitment of iron-catechol to the NGAL calyx should involve two steps: a bis-catecholate-iron complex would occupy first the pocket and then the addition of a third catecholate would form a tris-catecholate-iron complex stabilizing ferric iron. While the first step occurs at physiological pH (7.4), the second step is pH-independent [9].

The crystal structure of the NGAL-Fe(III)-catechol complex has iron coordinated by only one oxygen of a single catechol, a result of crystallization at pH 4.5 according to the speciation diagrams on the solution behavior of the Fe(III)-catechol system [9,11]. X-ray structures are also available for the wild type NGAL-enterobactin complex [6] and for two NGAL mutants with mutations in three residues lining the calyx complexed with enterobactin [12]. These crystal structures have allowed studying the lipocalin–enterobactin interaction [9,12,13] identifying key residues in the binding site. By using quadrupole moments obtained in *ab initio* calculations on model systems consisting of 1,2-hydroxypyrinidone and catecholamide units together with Na^+ and Ca^{2+} ions, it was concluded that a pivotal interaction occurs between cationic amino acids in the calyx and the π aromatic system of catechols [13]. However, the engineered variant that has several of these key residues in the calyx mutated is still able to bind iron chelators [5].

With the aim to address the sequential binding of isolated catechol, mono-, bis-, and tris-catecholate-iron ligands, we present here a computational study of Fe(III)-catechol species that constitute the main ligands of NGAL protein, the major lipocalin. This study intends to show that a modeling approach based on (1) quantum calculations to obtain structures, electron properties, and electrostatic potentials of Fe(III)-catecholate ligands, (2) flexible docking calculations to prepare protein–ligand complexes, and (3) Poisson–Boltzmann electrostatic potentials computed for proteins and ligands, is able to predict *in silico* reliable models of iron chelators binding. These models allow also to compare this binding between wild type NGAL protein and its largely modified engineered variant. Our work provides thus a modeling basis for the *in silico* research on variants of NGAL and related lipocalins, an issue which according to recent prospects [4,5,7] will be of interest in the immediate future.

2. Methods

2.1. Enterobactin and protein structures

Wild type NGAL geometry was taken from the X-ray structure of its complex with enterobactin (PDB code 1L6M) [6], actually represented in the crystal by DBS–DBH1–DBH2 (Fig. 1, DBS: 2,3-dihydroxy-benzoylserine, DBH: 2,3-dihydroxy-benzoic acid). NGAL engineered variant geometry was taken from its X-ray complex with the extracellular domain of human CTLA-4 (cytotoxic T lymphocyte-associated antigen 4) protein (PDB code 3BX7) [5]. Several engineered NGALs were derived from the human wild type upon constructing a mutant genetic library by randomizing 20 amino acid positions but the only crystallized variant was that having the best affinity to the T cell coreceptor CTLA-4 [5].

2.2. Quantum calculations

Structures of catechol, $[Fe(III)\text{-}(catecholate)_n]^{3-2n}$ ($n = 1–3$) and $[Fe(III)\text{-}H\text{-}catecholate]^{+2}$ species were optimized in quantum DFT calculations with the B3LYP hybrid functional and 6-311G(d,p) basis sets. Full geometry optimizations using analytic gradients without symmetry constraints were performed and frequencies analyzed to characterize minima. Octahedral high-spin Fe(III) was used [14]. Two further sets of B3LYP/6-311G(d,p) single-point calculations were performed at the optimized geometries to (1) compute atomic charges fit to the electrostatic potential at points selected according to the CHelpG scheme [15] and (2) obtain the electron density ρ (**r**) for topological analysis. All quantum calculations were performed with Gaussian 09 [16]. Critical points of ρ (**r**) were localized and characterized according to the Atoms in Molecules (AIM) theory [17,18] with Extreme [19]. 3D numerical grids of quantum electrostatic potentials were calculated with CheckDen [20] at spatial grids with 0.2 Å stepsize, converted to scalar OpenDX format and graphically rendered with PyMOL 1.5 [21].

2.3. Poisson–Bolztmann (PB) electrostatic potentials

PB electrostatic potentials were obtained with APBS 1.3 [22] assigning Amber99 charges [23] and atomic radii with Pdb2pqr 1.7 [24] to all atoms including hydrogens added to proteins and

optimized with this program. Ionic radius for octahedral Fe(III) was set at 0.785 Å [15]. PB potentials were obtained at 3D numerical grids with 0.2 Å stepsize for ligands and 0.4 Å stepsize for proteins by solving the nonlinear PB equation [25] in sequential-focusing multigrid calculations at 298.15 K, 0.150 M ionic strength, and dielectric constants 4 for proteins and 78.54 for water. Output numerical meshes were processed in scalar OpenDX format and graphically rendered with PyMOL 1.5 [21]. PB potential values are given in units of kT/e (k, Boltzmann's constant and e, unit charge; 1 kT/e = 2.48 kJ mol^{-1} at T = 298.15 K).

2.4. Protein–ligand dockings

Flexible dockings of catechol, [Fe(III)-(catecholate)$_n$]$^{3-2n}$ (n = 1–3), [Fe(III)-H-catecholate]$^{+2}$ isomers, and enterobactin were performed with AutoDock Vina [26]. AutoDock Tools 1.5.6 [27] was first used to prepare *pdbqt* files for proteins and ligands and to explore grid box settings. Taking the crystal structure of the NGAL-enterobactin complex [6] as a reference system, we set a 22 Å side cube box centered at the coordinates of Fe atom. This grid has the size recommended for a proper search space in Vina [26] and covers completely a large region around the calyx of lipocalins. Vina was then run to find all protein–ligand dockings and the solution showing the largest affinity (more negative energy) was chosen in all complexes.

2.5. Surface areas and protein–ligand interfaces

Solvent-accessible surface (SAS) areas were computed with the program LocaPep [28] which uses a new partition of surfaces obtained with the Arvomol numerical approach [29]. Protein ligand interfaces, hydrogen bonds (H-bonds) between protein amino acids and ligand atoms, and complex properties were obtained with the Protein Interfaces, Surfaces and Assemblies (PISA) software [30–32] using the EBIPISA server (www.ebi.ac.uk/msd-srv/prot_int/pistart.html).

3. Results

3.1. Structures of Fe(III)-catecholate ligands

Given the size and the number of the iron-containing species investigated and particularly the need to perform costly calculations to obtain quantum electrostatic potentials at fine spatial grids, we resorted to B3LYP/6-311G(d,p) DFT calculations. This choice was based upon the fairly good performance of this level of theory when compared with *ab initio* wave function-based correlated calculations to obtain geometries, electron properties and electrostatic potentials of compounds with aromatic rings [33,34]. Moreover, B3LYP/6-311G(d,p) calculations are known to provide results in good agreement with experimental data in the particular case of complexes of high-spin Fe(III) with organic cycles [35] and anionic ligands with a variety of negative charges [36–38] that include a spin-crossover system with one catecholate group [39]. These results demonstrate that the quantum methodology employed here shows a high degree of reliability compatible for positive and negative ions as well as neutral complexes of Fe(III).

For ease of notation, [Fe(III)-(catecholate)$_n$]$^{3-2n}$, n = 1–3, ligands will be herein denoted as follows: [Fe(III)-(catecholate)$_1$]$^{+1}$ = Fe(Cat)$_1$, [Fe(III)-(catecholate)$_2$]$^{-1}$ = Fe(Cat)$_2$, and [Fe(III)-(catecholate)$_3$]$^{-3}$ = Fe(Cat)$_3$. Although no symmetry constraints were imposed to optimize their geometries (Fig. 2A), Fe—O distances within a same ligand are identical (Table 1). Note, though, the significant difference between values ~2.06 Å with three bidentate ligands and the ~1.9 Å value with two or one bidentate ligands. If one compares these results with distances

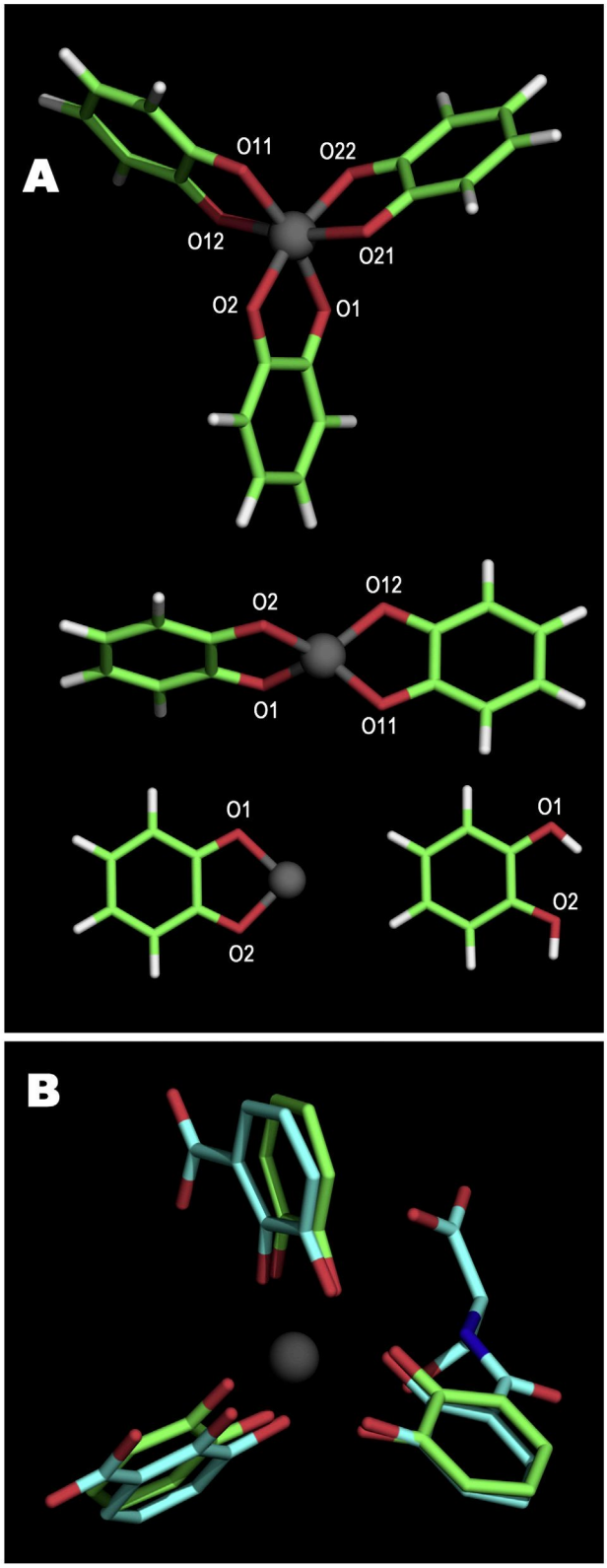

Fig. 2. (A) Iron catechol ligands at their B3LYP/6-311G(d,p) optimized geometries. Top, Fe(Cat)$_3$; middle, Fe(Cat)$_2$; bottom left, Fe(Cat)$_1$; bottom right, the most stable conformer of catechol. Stick diagrams with C, green; O, red; H, white; and Fe, dark gray. (B) Superposition of Fe(Cat)$_3$ geometry (green carbons) and X-ray geometry of enterobactin (cyan carbons) in its complex with wild type NGAL. (For interpretation of the references to color in this text, the reader is referred to the web version of the article.)

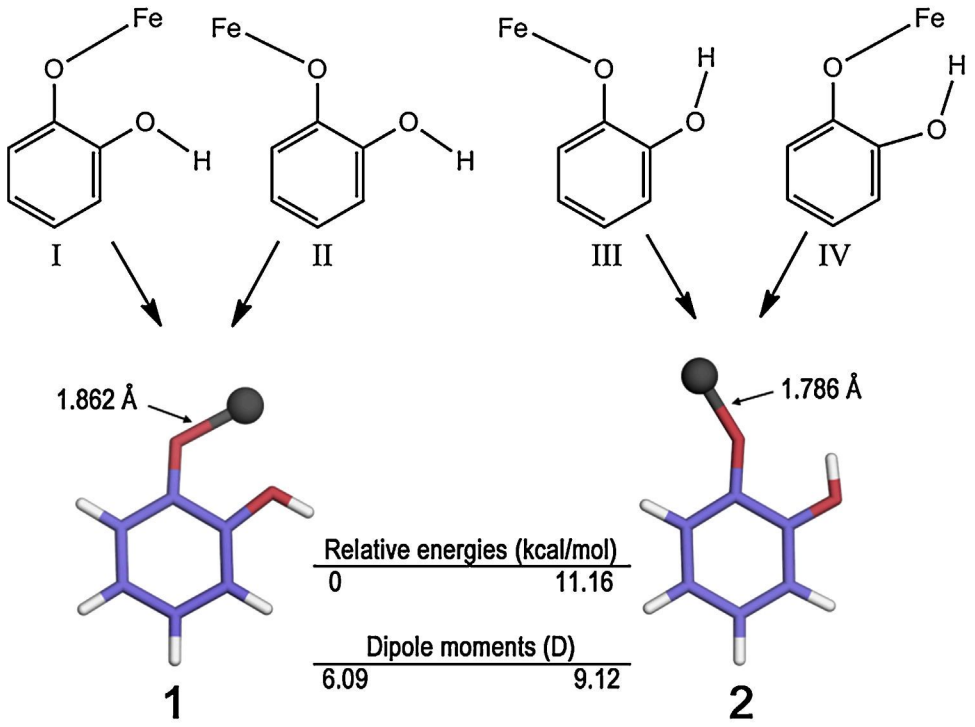

Fig. 3. Possible conformations of $FeH(Cat)_1$ (top) and optimized geometries found in B3LYP/6-311G(d,p) quantum calculations (bottom). Minimization of both initial geometries I and II led to isomer 1 while both III and IV led to isomer 2 (C, violet; O, red; H, white; Fe, dark gray). (For interpretation of the references to color in this text, the reader is referred to the web version of the article.)

observed in the X-ray structure, the regular hexacoordinate symmetry around iron is much more distorted in enterobactin. Superposition of quantum geometry of $Fe(Cat)_3$ and X-ray geometry of enterobactin in complex with wild type NGAL illustrates this point (Fig. 2B). The disparity of Fe—O distance values in enterobactin may be attributed to the network of H-bonds in the binding site: O atoms with distances longer than 2.0 Å participate in H-bonds with Y106, K125, and K134 residues at the site (see Fig. 7). More than 600 naturally occurring siderophores have been isolated and characterized [40]. Despite their great structural diversity, a common feature is the presence of hexacoordinate complexes with Fe(III), being the most frequent ligating groups O atoms of hydroxamate, catecholate, carboxylate, and mixed ligands. For comparison with distances in Table 1, the crystal structure of isolated triacetyl-fusarinine, a natural tris-(hydroxamate) complex, has Fe—O distances between 1.95 and 2.04 Å [40].

The recently published crystal structure of NGAL-catechol-Fe(III) complexes obtained at pH 4.5 has iron coordinated by only one oxygen of a single catechol [9]. We investigated the most stable conformers of this ligand, $[Fe(III)\text{-}H\text{-}catecholate]^{+2}$ ($FeH(Cat)_1$ in the notation introduced above) by means of B3LYP/6-311G(d,p) calculations. Unconstrained minimizations starting at the four possible initial conformations of substituted hydroxyls were found to lead to only two distinct isomers with large differences in energies and dipole moments (Fig. 3). The analysis of the crystal structure of NGAL-catechol-Fe(III) complex reveals that the ligand corresponds to our isomer with the greatest dipole moment (2 in Fig. 3). In fact, Fe—O distance in the ligand of this crystal complex (1.792 Å) [9] and our value for isomer 2 (1.786 Å) are nearly identical. It should also be noted that C—O—Fe bond angles in $FeH(Cat)_1$ (120.8° and 145.1° in isomers 1 and 2, respectively) differ significantly from those in $Fe(Cat)_n$ structures: 114.4° in $Fe(Cat)_3$, 110.3° in $Fe(Cat)_2$, and 108.5° in $Fe(Cat)_1$. It is tempting to assume that longer Fe—O distances (Table 1) might be associated to a relaxing effect against bond angle strain in C—O—Fe—O—C closed rings.

3.2. Electron properties of Fe(III)-catecholate ligands

Computed atomic charges and dipole moments are collected in Tables S1 and S2 of the Supplementary Material. Total charges are: −3 for $Fe(Cat)_3$ and enterobactin, −1 for $Fe(Cat)_2$, +1 for $Fe(Cat)_1$, +2 for both $FeH(Cat)_1$ isomers, and 0 for catechol. As expected by symmetry, quantum calculations give zero dipole moments for ligands with three and two catecholates while $Fe(Cat)_1$ has $\mu = 5.45$ D (clearly smaller than μ values for $FeH(Cat)_1$ isomers, Fig. 3) and catechol 2.47 D, in excellent agreement with the experimental value,

Table 1
Fe^{3+}-oxygen distances in enterobactin and Fe(III)-catecholate ligands.[a]

Enterobactin in complex with wild type NGAL. X-ray data (1L6 M)					
$O3_{DBH1} = 1.806$	$O6_{DBH1} = 2.325$	$O3_{DBH2} = 1.889$	$O6_{DBH2} = 2.031$	$O1_{DBS} = 2.234$	$O4_{DBS} = 2.322$
Isolated $Fe(Cat)_3$. B3LYP/6-311G(d,p) geometry					
O1 = 2.056	O2 = 2.058	O11 = 2.057	O12 = 2.057	O21 = 2.056	O22 = 2.058
Isolated $Fe(Cat)_2$. B3LYP/6-311G(d,p) geometry					
O1 = 1.894	O2 = 1.894	O11 = 1.894	O12 = 1.894		
Isolated $Fe(Cat)_1$. B3LYP/6-311G(d,p) geometry					
O1 = 1.897	O2 = 1.897				

[a] Labeling of O atoms refers to Figs. 1 and 2. Distances in Å.

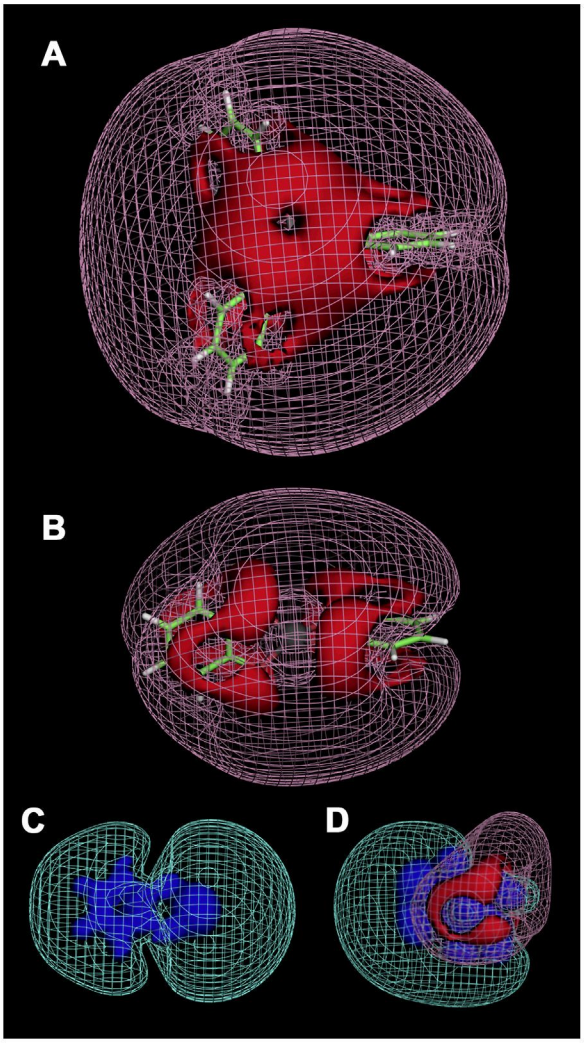

Fig. 4. Quantum electrostatic potential isosurfaces of iron catechol ligands at the geometries shown in Fig. 2. (A) $Fe(Cat)_3$ isosurfaces −400 (solid, red) and −200 (mesh, pink). (B) $Fe(Cat)_2$ isosurfaces −200 (solid, red) and −100 (mesh, pink). (C) $Fe(Cat)_1$ isosurfaces +400 (solid, blue) and +100 (mesh, cyan). (D) catechol isosurfaces −50 (solid, red), −10 (mesh, cyan), +50 (solid, blue), and +10 (mesh, cyan). All values in kT/e units. (For interpretation of the references to color in this text, the reader is referred to the web version of the article.)

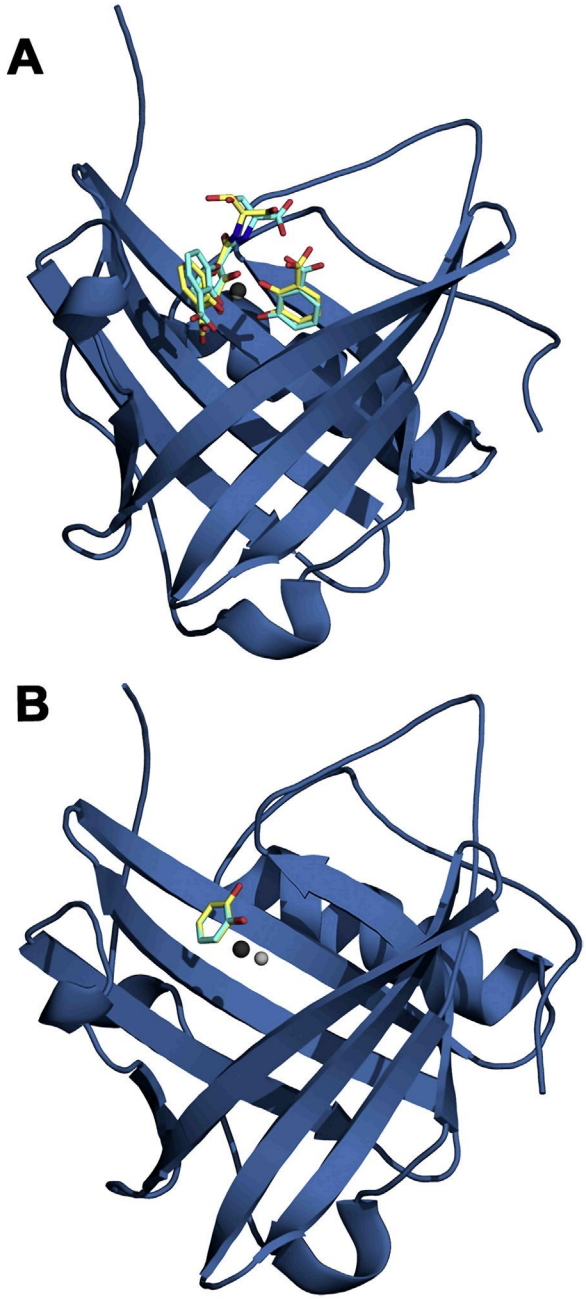

Fig. 5. Superposition of crystal and docked structures of wild type NGAL-ligand complexes. Ligands in crystal structures shown as stick diagrams with C atoms in cyan and Fe in dark gray. Docked ligands shown as stick diagrams with C atoms in yellow and Fe in light gray. A. NGAL-enterobactin complex (1L6M). (B) NGAL-Fe(III)-catechol complex (3FW4). (For interpretation of the references to color in this text, the reader is referred to the web version of the article.)

2.62 ± 0.03 D [41]. However, the spatial distribution of charge provides a more interesting information (Fig. 4). In what follows, it should be recalled that atomic charges were computed to fit the electrostatic potential.

The quantum electrostatic potential in $Fe(Cat)_3$ is characterized by highly negative isovalues that outline the trigonal symmetry of catecholate rings around iron (solid surface in Fig. 4). They are originated at six oxygen atoms with atomic charges about $-0.71e$ which, added to the atomic charge $+1.76e$ of iron yields a net charge $-2.50e$ in the FeO_6 moiety. Hence, the three aromatic rings contribute $-0.50e$ to the total negative charge −3. As expected, lower isovalues (meshed surface in Fig. 4) display nearly spherical symmetries. The quantum electrostatic potential in $Fe(Cat)_2$ is also predominantly negative but now exhibits lower isovalues than $Fe(Cat)_3$ around nuclear positions. Oxygen atomic charges -0.76e and iron charge $+1.72e$ yield in $Fe(Cat)_2$ a net charge $-1.32e$ in FeO_4 moiety which means that the two aromatic rings now contribute $+0.32e$ to the total negative charge −1. $Fe(Cat)_1$ is characterized by strongly positive potential isovalues that outline separately carbon ring and O—Fe—O moieties. Oxygen atomic charges are now $-0.78e$, iron charge is $+1.59e$ and the net charge in the FeO_2 moiety is thus essentially zero so that the aromatic ring contributes now the total positive charge +1. For comparison, neutral catechol shows a well differentiated electrostatic behavior with positive domains arising from the carbon ring and negative isosurfaces outlining hydroxyls. Total zero charge is now split in $-0.31e$ for hydroxyls and $+0.31e$ for the aromatic ring.

The topological analysis of the electron density $\rho(\mathbf{r})$ [17,18] provides information of interest on the bonding nature of Fe···O interactions. Topological descriptors of bond critical points (BCPs) of $\rho(\mathbf{r})$ at Fe···O bond paths (ρ_C in Table 2) are typical of closed-shell, non-covalent interactions but also exhibit some degree of covalent character, particularly in ligands with two and one catecholates.

Table 2
Topological descriptors of bond critical points (BCPs) of the electron density at Fe···O bond paths in Fe(Cat)$_n$ ligands. B3LYP/6-311G(d,p) calculations.[a]

Bond	Fe—O1	Fe—O2	Fe—O11	Fe—O12	Fe—O21	Fe—O22
Fe(Cat)3						
ρ_C	0.0737	0.0733	0.0734	0.0735	0.0736	0.0734
$\nabla^2\rho_C$	0.3499	0.3470	0.3481	0.3482	0.3495	0.3480
G_C	0.0911	0.0903	0.0906	0.0907	0.0910	0.0906
V_C	−0.0948	−0.0938	−0.0942	−0.0943	−0.0947	−0.0942
Fe(Cat)2						
ρ_C	0.1127	0.1127	0.1127	0.1127		
$\nabla^2\rho_C$	0.5590	0.5589	0.5590	0.5589		
G_C	0.1615	0.1614	0.1615	0.1614		
V_C	−0.1832	−0.1832	−0.1832	−0.1832		
Fe(Cat)1						
ρ_C	0.1097	0.1097				
$\nabla^2\rho_C$	0.5639	0.5638				
G_C	0.1608	0.1608				
V_C	−0.1806	−0.1806				

[a] Descriptors computed at the BCP: ρ_C is the electron density, $\nabla^2\rho_C$ is the Laplacian of the electron density, G_C is the kinetic energy density, and V_C is the potential energy density. All values in atomic units. Atom numbering refers to Fig. 2.

The magnitude of ρ_C (~0.073 a.u. in Fe(Cat)$_3$ and ~0.110 a.u. in both Fe(Cat)$_2$ and Fe(Cat)$_1$) as well as the positive sign of the Laplacian of $\rho(\mathbf{r})$ at the BCP $\nabla^2\rho_C$, a feature of paths with local depletion of charge, are indicative of non-covalent strong interactions such as ionic attractions or very strong hydrogen bonds [17,18]. However, the magnitude of $\nabla^2\rho_C$ (+0.348 a.u. in Fe(Cat)$_3$ and +0.560 a.u. in both Fe(Cat)$_2$ and Fe(Cat)$_1$) is reminiscent of strong interatomic attractions such as those observed at intermediate distances between non-covalent and covalent bonds in proton transfer in very strong H-bond complexes [42–46]. In these cases, it is known that positive $\nabla^2\rho_C$ increases at shorter interatomic distances, reaches a maximum and then decreases rapidly becoming negative (a covalent feature) at a "critical" distance which separates covalent and non-covalent domains [42–44]. As far as this descriptor is concerned, the comparison of $\nabla^2\rho_C$ values (Table 2) with Fe—O distances (Table 1) suggests that both Fe(Cat)$_2$ and Fe(Cat)$_1$ are closer to the covalent regime than Fe(Cat)$_3$.

Further evidence is provided by total energy density H_C values. H_C is the sum of the always positive (repulsive) kinetic energy density G_C and the always negative (attractive) potential energy density at the BCP V_C. Therefore, the sign of $H_C = G_C + V_C$ indicates what is the dominant contribution at the BCP. G_C dominates in non-bonded interactions whereas V_C does it in covalent bonds. The presence of $H_C < 0$ in an interatomic path of a non-bonded case is usually interpreted as a proof of strong interaction and some degree of covalent character is then assumed as it occurs in strong H-bonds [18,44–47]. G_C and V_C values for Fe···O paths in Fe(Cat)$_n$ ligands (Table 2) yield $H_C \sim -0.004$ a.u. in Fe(Cat)$_3$ and ~ -0.020 a.u. in both Fe(Cat)$_2$ and Fe(Cat)$_1$. Even though all H_C values are negative, their different magnitude suggests again that a clear covalent character might be attributed to Fe—O interactions in Fe(Cat)$_2$ and Fe(Cat)$_1$ but not in Fe(Cat)$_3$.

3.3. Protein–ligand dockings

Flexible docking is achieved in AutoDock Vina throughout the rotatable bonds of the ligand. In a successful run the program gives several solutions ranked by decreasing affinity energy. These predicted affinities were found to correlate with experimental binding energies with a standard error about 2.7 kcal mol^{-1} for a dataset of 116 protein–ligand complexes [26]. Before presenting docking results it must be recalled that crystal structures of wild type NGAL as well as mutants complexed with enterobactin revealed that the conformation is not affected neither locally nor globally by these changes of residues [12]. Even the engineered variant which has up to 20 amino acids mutated shows the same backbone conformation than wild type NGAL (RMSD computed with backbone atoms in the superposition is 0.76 Å) [5].

Table 3
PISA protein–ligand interface properties and predicted binding affinities for best dockings of NGAL protein-catecholates complexes obtained with Vina.[a]

Ligand	Surface area	Buried area	$\Delta^{int}G$	$T\Delta S^{diss}$	E^{aff}
Wild type					
Catechol	9468	311.0	5.5	1.4	−5.2
FeH(Cat)$_1$ isom.1	9443	376.6	5.1	2.3	−5.6
FeH(Cat)$_1$ isom.2	9445	376.8	5.0	2.3	−5.6
Fe(Cat)$_1$	9458	346.2	4.8	2.1	−5.7
Fe(Cat)$_2$	9444	495.0	4.5	3.5	−8.1
Fe(Cat)$_3$	9329	734.0	2.9	4.5	−11.0
Enterobactin[b]	9378	770.6	1.1	5.0	−11.7
Enterobactin[c]	9368	767.9	1.2	5.0	–
Engineered variant					
Catechol	9440	293.9	3.1	1.4	−4.7
FeH(Cat)$_1$ isom.1	9434	341.7	2.6	2.3	−5.0
FeH(Cat)$_1$ isom.2	9431	340.5	2.8	2.3	−5.0
Fe(Cat)$_1$	9436	321.4	2.9	2.1	−5.6
Fe(Cat)$_2$	9391	502.4	2.0	3.5	−6.8
Fe(Cat)$_3$	9383	633.6	0.8	4.5	−8.2
Enterobactin	9362	749.0	−1.5	5.0	−8.7

[a] Surface area is the SAS area of the complex, buried area is the SAS area buried upon formation of the complex, $\Delta^{int}G$ is the solvation free energy gain upon formation of the interface, $T\Delta S^{diss}$ is the rigid-body entropy change energy at complex dissociation at 298 K, and E^{aff} is the binding affinity of the best Vina docking. Areas in Å^2, energies in kcal mol^{-1}.
[b] Docked structure.
[c] X-ray crystal structure (PDB code 1L6M)

The comparison between structures obtained at docking calculations and the equivalent crystal structures demonstrates the excellent performance of Vina in providing reliable geometries for these protein–ligand complexes (Figs. 5–7 and Table 3). Docked structures predict the correct binding site at the calyx and show nearly coincident geometries for ligands (Figs. 5 and 6). 20 residues (Table S3 of the Supplementary Material) are found to be within 4 Å of ligands in both wild type and engineered NGAL proteins. Out of these 20 amino acids, 16 are at or near the binding site and out of these, only 6 are within 3 Å of ligands in either crystal or docked structures (Table S3). In the wild type protein these 6 residues (W79, R81, Y100, Y106, K125, and K134) form a double patch spanning a small region of the pocket surface (Figs. 6 and 8). The engineered variant has 4 of these residues mutated (W79T, R81A, K125L, and K134A) and therefore amino acids within 3 Å of the ligand differ (Table S3). They are: R40 (mutated from wild type

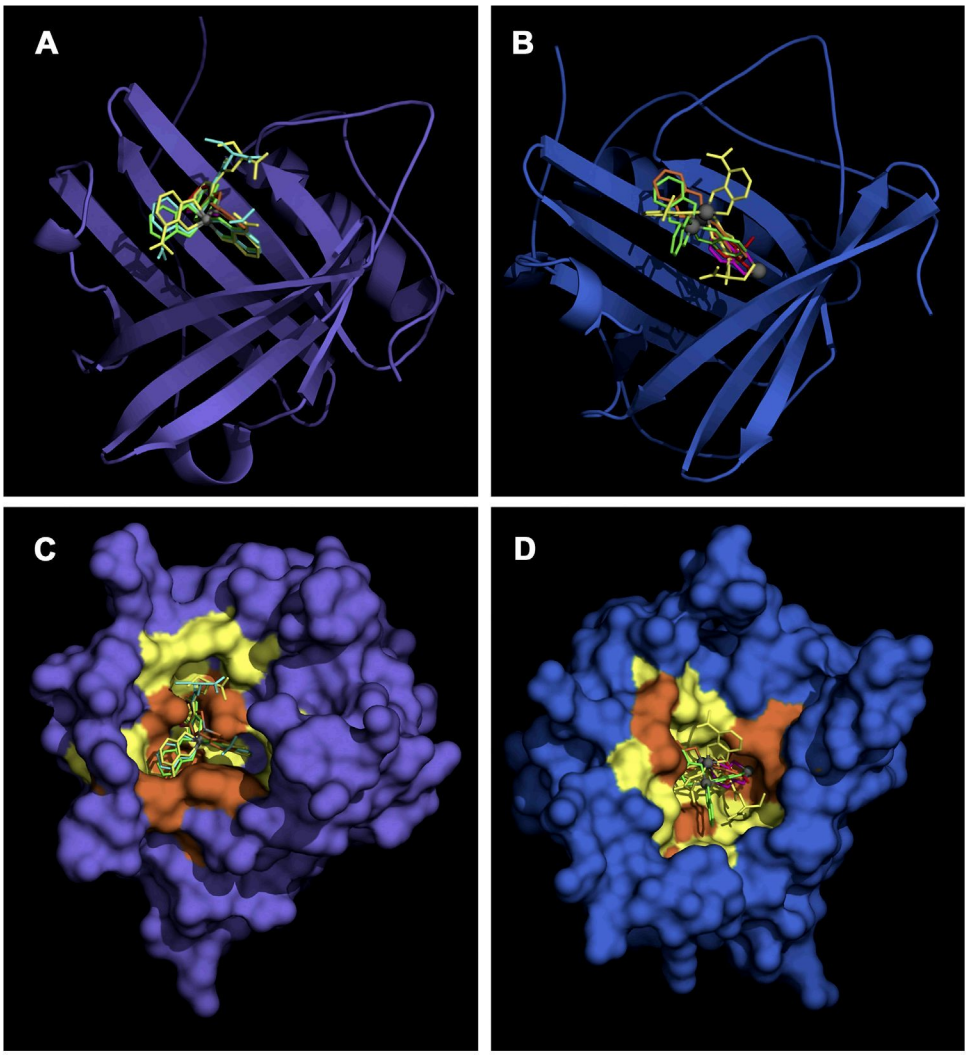

Fig. 6. Top, ribbon diagrams of wild type NGAL protein (A) and its engineered variant (B) showing the binding site (the "calyx") of the following ligands (sticks): enterobactin in the crystal structure of its complex with NGAL (cyan), docked enterobactin (yellow), and docked $Fe(Cat)_3$ (green), $Fe(Cat)_2$ (orange), $Fe(Cat)_1$ (magenta), and catechol (red). Bottom, molecular surfaces showing areas of residues within 4 Å (yellow) and 3 Å (orange) of the ligands in wild type NGAL protein (C) and its engineered variant (D). (For interpretation of the references to color in this text, the reader is referred to the web version of the article.)

A40), Y52, T54, S68, Y106, and Y138 (Fig. 8). It is noteworthy that in spite of the many changes that affect the binding site, 6 amino acids define also this close 3 Å neighborhood although they are now more scattered over the pocket surface than in the wild type protein (Fig. 6). Note, though, the presence of tyrosines, aromatic and basic amino acids in both cases (Fig. 8). If one compares the binding site topography in the two NGALs clear differences are seen. Wild type protein has a pocket with three deep wells spanning a smaller region than the engineered protein which has a shallow pocket covering a larger area (Fig. 6). As a consequence, protein-ligand interface SAS areas (Table S4 of the Supplementary Material) are noticeably greater in the former protein than in the latter.

A network of H-bonds between catechol oxygens and residues at the calyx are identified (Fig. 7). Since the docked structure reproduces fairly well the H-bond network in the crystal structure of wild type NGAL-enterobactin complex, one can reasonably assume the validity of hydrogen bonding data for the remaining ligands. In the wild type protein this network arises exclusively from three amino acids which arrange around the octahedral Fe(III)-oxygens moiety to anchor it: Y106, K125, and K134. As for the two tris-catecholate ligands, the presence of other oxygens besides those in catechol groups allows for an additional H-bond in enterobactin (K125-NZ···O13) absent in $Fe(Cat)_3$ (Fig. 7A and B). It is interesting to see how docking calculations optimize binding in this case: although ligand geometries are rather similar, a slight shift of the tris-catecholate moiety permits two extra H-bonds with Y106 and K125. It must be also emphasized that short distances in some of these H-bonds suggest very strong links: see for example two N···O distances ~2.5 Å for K125 and K134 in enterobactin. Less H-bonds and slightly longer distances that suggest a bit weaker attractions contribute to bind $Fe(Cat)_3$ (Fig. 7C). As for bis- and mono-catecholate ligands, docked structures reveal the existence of H-bonds that link catechol oxygens to the same amino acids: K125 and K134 in $Fe(Cat)_2$, Y106 and K134 in $Fe(Cat)_1$, and the three of them in catechol. As expected from the smaller size of these two latter ligands, H-bond distances become longer than in the tris-catecholate case (Fig. 7D–F). In sharp contrast, engineered NGAL shows a few H-bonds linking tris- and bis-catecholate ligands although both $Fe(Cat)_1$ and catechol are bound with a nearly identical H-bond network (Table S5 in the Supplementary material).

Protein–ligand interface properties computed with PISA (Table 3) for the best docked complex structures reveal positive solvation free energy gain upon formation of the interface

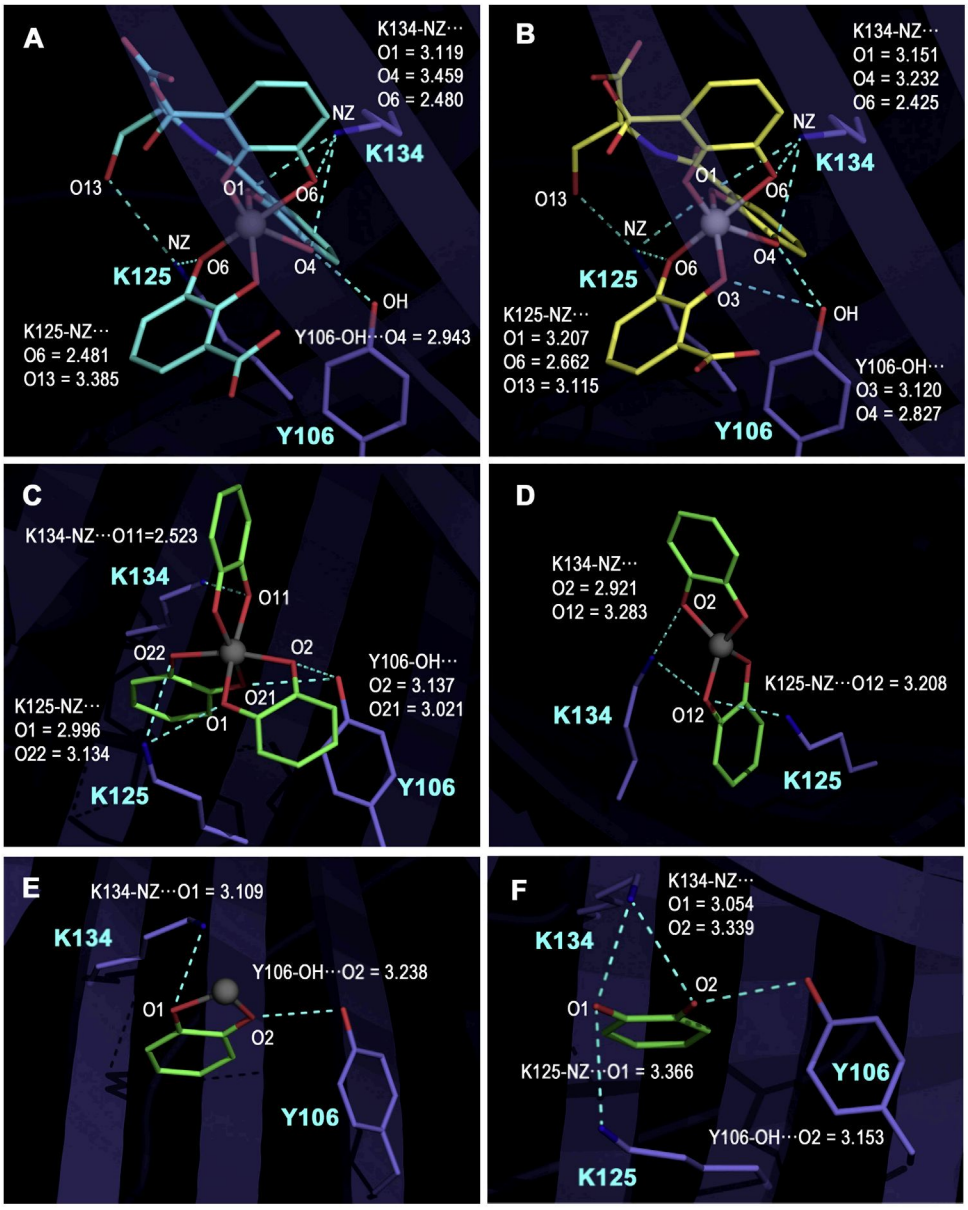

Fig. 7. Hydrogen bonds (cyan dashed line) between Fe(III) (gray.spheres)-catecholate ligands and residues (violet sticks) in wild type NGAL at the binding site (distances in Å). (A) Enterobactin in the crystal structure. The remaining panels correspond to docked structures. (B) Enterobactin, (C) $Fe(Cat)_3$, (D) $Fe(Cat)_2$, (E) $Fe(Cat)_1$, (F) Catechol. (For interpretation of the references to color in this text, the reader is referred to the web version of the article.)

$\Delta^{int}G$ for all catecholate ligands. Given that this property is computed in PISA as difference in total solvation energies between isolated and assembled (interfacing) structures, positive $\Delta^{int}G$ values mean negative contributions to the solvation energy gain of the interface, which corresponds to hydrophobic effect [30,32]. Since protein–catecholates interactions at the binding site are strongly dominated by local electrostatic interactions at the calyx that increase with the number of catecholate moieties coordinating iron (see below), positive $\Delta^{int}G$ values in Table 3 decrease accordingly. PISA computes entropy contribution to the free energy of complex dissociation $T\Delta S^{diss}$ in terms of a rigid-body entropy model plus entropy of surface atoms with fractional degrees of freedom [32]. As expected, these energies increase in Table 3 with the size of the ligand and roughly indicate an increase of about 1 kcal mol^{-1} per catecholate ring. Because the two sets of values in Table 3 correspond to same ligands in proteins with same structure, they are coincident. Surface areas for the whole complexes decrease very little with the increasing size of ligands yet this tiny contraction effect is negligible when compared with the large variations noticed in buried areas which increase from about 300 Å^2 in catechol to 770 Å^2 in enterobactin. This significant variation must obviously be related not only with the observed decrease in $\Delta^{int}G$ values but also with greater protein–ligand affinities as discussed below. Note again the close agreement between docked and crystal structure data for the wild type NGAL-enterobactin complex with regard to PISA properties.

Trends observed in binding affinities for best dockings in Vina calculations (E^{aff} column in Table 3) indicate that affinity increases with the number of catecholate rings. Ligands with a single aromatic ring display $E^{aff} \sim -5$ kcal mol^{-1} regardless the protein. It is also noticed that the presence of Fe(III) ion has little effect on E^{aff} values: if one compares $FeH(Cat)_1$ isomers or $Fe(Cat)_1$ affinities with that of catechol, they differ in only a few tenths of kcal mol^{-1}. Engineered NGAL shows lower affinities, particularly to ligands with more than one catecholate ring. The above mentioned correlation of Vina predicted affinities with experimental binding energies

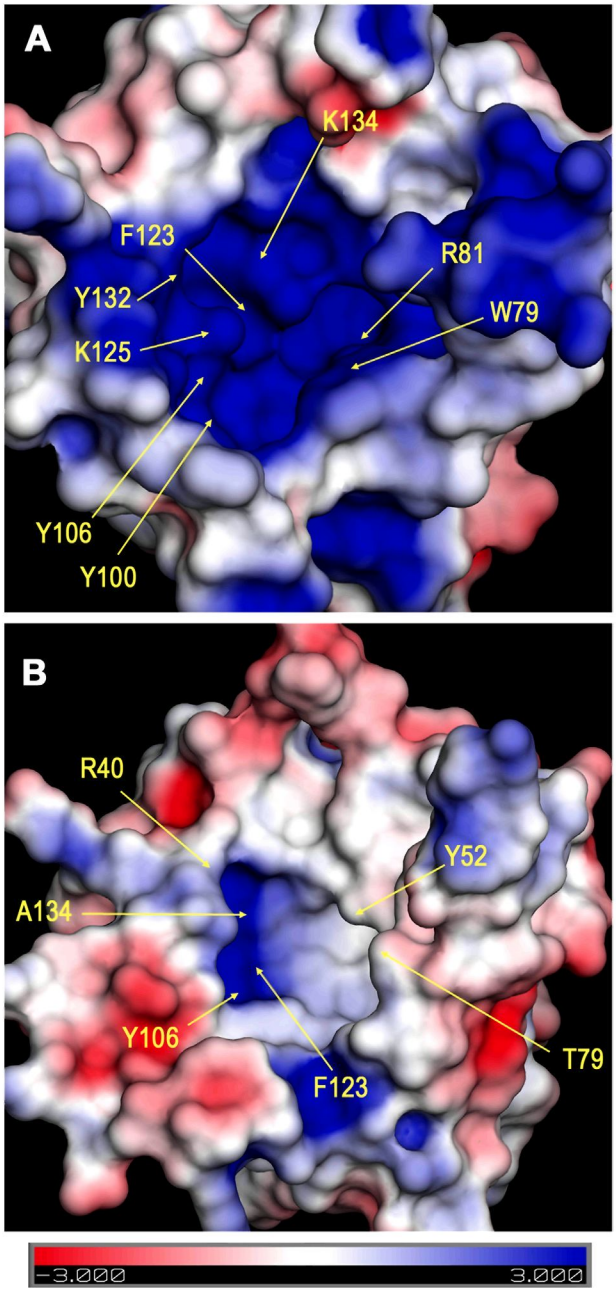

Fig. 8. Poisson–Boltzmann electrostatic potential mapped onto the molecular surface at the calyx of NGAL proteins. (A) Wild type. (B) Engineered variant.

[26] and the fact that calculated binding constants for catechol and $Fe(Cat)_2$ bound to wild type NGAL indicates binding free energies about −9.1 and −11.8 kcal mol^{-1}, respectively, [9] permit to see these E^{aff} values as rough estimates of protein–ligand binding.

3.4. Poisson–Boltzmann electrostatic potentials

The pocket in wild type NGAL shows outstanding electrostatic differences with respect to the remaining surface as it is characterized by a strongly positive PB electrostatic potential with little (if any) local differences (Fig. 8A). This positive potential is produced by the structural convergence of basic amino acids, particularly R81, K124 (nearly completely buried in the bottom of the pocket), K125 and K134. In contrast, the engineered variant has rather different electrostatic features. In this protein, R40 (non-engineered A40) and buried K124 produce the positive region seen at the bottom

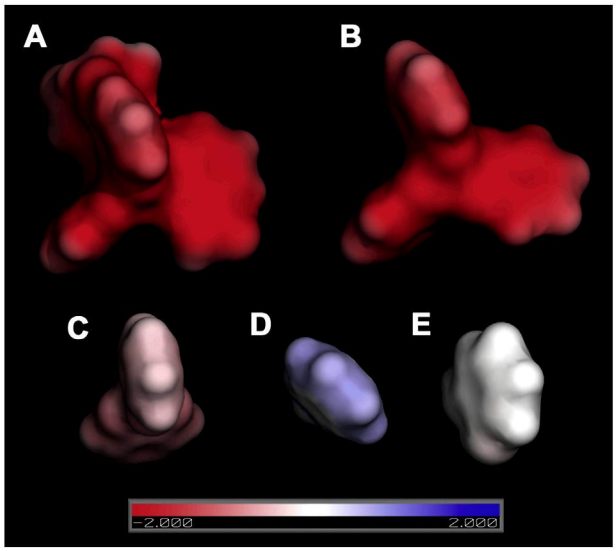

Fig. 9. Poisson–Boltzmann electrostatic potential mapped onto the molecular surface of ligands. (A) Enterobactin, (B) $Fe(Cat)_3$, (C) $Fe(Cat)_2$, (D) $Fe(Cat)_1$, (E) catechol. In all cases, front view corresponds to the surface in contact with binding sites shown in Fig. 8.

of the pocket but R81A, K125L, and K134A mutations modify completely the electrostatic potential at the site which shows now a predominantly neutral surface (Fig. 8B). As discussed above, a further difference concerns the own shape of the pocket. Comparing with the wild type case, the pocket in the engineered variant is considerably smaller and features a rather modified shape.

Iron catecholate ligands show dramatic differences in their PB electrostatic potentials (Fig. 9) that parallel their total electric charge. Enterobactin is completely negative to such an extent that not a single patch with neutral potential is seen over its whole surface. As expected, and besides similar own spatial shapes, $Fe(Cat)_3$ (total charge −3) exhibits a negative potential nearly identical to that of enterobactin. The electrostatic complementarity between these negative ligands and the positive pocket in the wild type protein is fairly evident. $Fe(Cat)_2$ (total charge −2) is slightly negative whereas $Fe(Cat)_1$ (total charge +1) and catechol (total charge 0) show positive and neutral electrostatic potentials, respectively.

4. Discussion

The essential role played by NGAL protein in binding iron chelators may help to elucidate still unknown pathways of iron transport. Its affinity to enterobactin, the archetype of siderophores, provides clues to understand the special binding abilities of this lipocalin which are instrumental in defense mechanisms against bacterial infection [4–9]. Recent reports showing that catechols, small metabolites able to bind iron, permit effective sequestration and transport of iron by NGAL [9], have widened the scope of the analysis on the interactions occurring in the binding site of this remarkable protein. By studying these interactions between Fe(III)-catechol ligands and the wild type form together with an engineered variant with relevant modifications in the binding site, we present computational results that provide information of interest for the binding to lipocalins of these iron ligands.

Quantum calculations on catechol and Fe(III)-mono-, bis-, and tris-catecholate ligands predicted stable structures coordinating Fe^{3+} ion. The analysis of the electron density revealed features of covalent bonding in Fe···O interactions in ligands with one- and two-bidentate catecholate rings. In contrast, features on non-covalent, strong ionic attractions dominate the Fe···O interaction in

ligands with three catecholate rings. Both characteristics are supported by geometry data, particularly Fe—O distances significantly shorter in $Fe(Cat)_2$ and $Fe(Cat)_1$ than in $Fe(Cat)_3$. Whereas catechol is moderately polar (μ = 2.47 D), Fe(III)-mono-catecholates are strongly polar: μ = 6.09 and 9.12 D in the two isomers of $FeH(Cat)_1$ and μ = 5.45 D in $Fe(Cat)_1$. On the contrary, $Fe(Cat)_2$ and $Fe(Cat)_3$ are non-polar by symmetry.

Total charges are 0 in catechol, +2 in the isomers of $FeH(Cat)_1$, +1 in $Fe(Cat)_1$, −1 in $Fe(Cat)_2$, and −3 in both $Fe(Cat)_3$ and enterobactin. Furthermore, charge effects arising from Fe(III)-oxygen coordination structures and to a lesser extent aromatic rings should also contribute. FeO_2 moiety in mono-catecholate ligand has zero net charge, FeO_4 moiety in $Fe(Cat)_2$ has net charge $-1.32e$, and the FeO_6 coordination structure in $Fe(Cat)_3$ has net charge $-2.50e$. Besides, the single aromatic ring in catechol and $Fe(Cat)_1$ has positive net charge $+0.31e$ and $+1e$, respectively, the two rings in $Fe(Cat)_2$ have also positive net charge $+0.32e$ while the three aromatic rings in $Fe(Cat)_3$ contribute a negative total net charge $-0.50e$. This feature agrees with the proposal of cation-π interactions arising from basic amino acids in the calyx [9,13] in the tris-catecholate case. Hence, the key role played by monopole effects and the greater affinity to bis- and tris-catecholates than to mono-catecholate ligands rule out any significant participation of dipole moment effects in the interactions with proteins.

The spatial distribution of charge provided by quantum electrostatic potentials give crucial information to understand the distinct binding affinity of these iron catecholate ligands. Only the presence of three catechol rings gives rise to a uniform strongly negative electrostatic potential as it is found in the Fe(III)-tris-catecholate species. Fe(III)-bis-catecholate has a much weaker negative potential and the remaining one-catechol ligands show either neutral or positive quantum potentials. All these features are also present in Poisson–Boltzmann electrostatic potentials calculated for Fe(III)-catecholates ligands and for the siderophore enterobactin that exhibits a completely negative PB potential nearly identical to $Fe(Cat)_3$ over its whole surface.

As for the binding pocket of these proteins (the "calyx"), spatial charge distributions represented by PB electrostatic potentials that incorporate solvation and ionic solution effects provide information of paramount importance to understand the binding abilities of lipocalins. In wild type NGAL, this binding pocket is characterized by a remarkably uniform, strongly positive electrostatic potential thanks to the spatial convergence of basic side chains of K124 (nearly buried at the bottom of the pocket), K125, K134, and to a lesser extent, R81. It is thus apparent that regardless the particular protein–ligand interactions occurring at the calyx, the strong electropositive nature of the binding site must create a long reaching attractive effect on electrostatically negative ligands. In contrast, the engineered variant designed to bind to the T cell coreceptor CTLA-4 has the mutations R81A, K125L, and K134A in the binding site and therefore exhibits a different electrostatic potential at the calyx although it still shows a small positive region amidst a predominantly neutral pocket.

Accurately predicting protein–ligand binding free energies remains an open problem in computational chemistry. Reliable methods to obtain protein-ligand binding constants based upon molecular dynamics (MD) calculations do exist [48]. However, MD procedures face a still unsolved complication: the need to generate accurate parameters for the ligand within the force field considered. While a satisfactory general solution has been found when the ligand is a small organic molecule [49], the presence of a metal poses a major problem especially for obtaining force field terms depending on vibrational modes. And this is particularly difficult in cases such as the iron-catecholate ligands studied here for which even two distinct types of bonding with a clearly different covalent contribution between metal and chelating atoms have been found.

Given that docking Vina calculations provide structures and properties that reproduce fairly well existing experimental evidence for the wild type NGAL-enterobactin complex, we used the docked structures to explore the interactions with Fe(III)-catecholate ligands with the help of PISA analyses of protein-ligand interfaces. Binding affinities given by flexible docking calculations agree reasonably with the trends expected from charge/electrostatic considerations. Increasingly negative iron chelators $Fe(Cat)_2$, $Fe(Cat)_3$, and enterobactin show increasingly greater binding affinities in the wild type NGAL protein. Besides long-range electrostatic effects, a network of hydrogen bonds arising mainly from three residues in the calyx, Y106, K125, and K134, are found to bind catecholate ligands by linking the oxygen atoms that coordinate ferric ion. The engineered variant has R81A, K125L, and K134A mutations that affect key residues in binding enterobactin and Fe(III)-catecholates and therefore this protein shows a lower affinity to ligands with aromatic rings.

In conclusion, our results indicate that the calyx of the NGAL protein is a particularly efficient site to bind iron chelators with catechol groups coordinating Fe(III). Charge effects arising from the strongly positive electrostatic potential at the binding site make it particularly suitable to bind ligands with strongly negative electrostatic potentials. This feature is characteristic of iron chelators with at least two and especially three aromatic rings providing hexacoordinate catechol oxygens. In addition, we propose the existence of a network of hydrogen bonds formed by a few key amino acids in the calyx able to stabilize the binding by linking iron-chelating oxygen atoms. Our results complement the proposal of cation-π interactions [9,13] in the calyx of lipocalins and cast light on protein–ligand interactions occurring in these remarkable proteins.

Acknowledgments

This research is funded by Spanish Ministerio de Ciencia e Innovación, contract grant BIO2009-0705. C.G.C. is supported by a grant from the Spanish FPI program. E.J.J. and F.R.W. are supported by the Austrian National Fund FWF grant SFB 4606-B19.

Appendix A. Supplementary data

Supplementary data associated with this article can be found, in the online version, at http://dx.doi.org/10.1016/j.jmgm.2013.08.013.

References

[1] D.R. Flower, A.C.T. North, T.K. Attwood, Structure and sequence relationships in the lipocalins and related proteins, Protein Sci. 2 (1993) 753–761.
[2] D.R. Flower, A.C.T. North, C.E. Sansom, The lipocalin protein family: structural and sequence overview, Biochim. Biophys. Acta 1482 (2000) 9–24.
[3] A. Skerra, Lipocalins as a scaffold, Biochim. Biophys. Acta 1482 (2000) 337–350.
[4] S. Chakraborty, S. Kaur, S. Guha, S.K. Batra, The multifaceted roles of neutrophil gelatinase associated lipocalin (NGAL) in inflammation and cancer, Biochim. Biophys. Acta 1826 (2012) 129–169.
[5] D. Schönfeld, G. Matschiner, L. Chatwell, S. Trentmann, H. Gille, M. Hülsmeyer, N. Brown, P.M. Kaye, S. Schlehuber, A.M. Hohlbaum, A. Skerra, An engineered lipocalin specific to CTLA-4 reveals a combining site with structural and conformational features similar to antibodies, Proc. Natl. Acad. Sci. USA 106 (2009) 8198–8203.
[6] D.H. Goetz, M.A. Holmes, N. Borregaard, M.E. Bluhm, K.N. Raymond, R.K. Strong, The neutrophil lipocalin NGAL is a bacteriostatic agent that interferes with siderophore-mediated iron acquisition, Mol. Cell 10 (2002) 1033–1043.
[7] K. Pantopoulos, S.K. Porwal, A. Tartakoff, L. Devireddy, Mechanisms of mammalian iron homeostasis, Biochemistry 51 (2012) 5705–5724.
[8] K.N. Raymond, E.A. Dertz, S.S. Kim, Enterobactin, An archetype for microbial iron transport, Proc. Natl. Acad. Sci. USA 100 (2003) 3584–3588.
[9] G. Bao, M. Clifton, T.M. Hoette, K. Mori, S.X. Deng, A. Qiu, M. Viltard, D. Williams, N. Paragas, T. Leete, R. Kulkarni, X. Li, B. Lee, A. Kalandadze, A.J. Ratner, J. Pizarro, K.M. Schmidt-Ott, D.W. Landry, K.N. Raymond, R.K. Strong, J. Barasch, Iron traffics in circulation bound to a siderocalin (NGAL)-catechol complex, Nat. Chem. Biol. 6 (2010) 602–609.

[10] S.G. Carmella, V.E.J. La, S.S. Hecht, Quantitative analysis of catechol and 4-methylcatechol in human urine, Food Chem. Toxicol. 20 (1982) 587–590.
[11] Z.D. Liu, R.C. Hider, Design of iron chelators with therapeutic application, Coord. Chem. Rev. 232 (2002) 151–171.
[12] R.J. Abergel, M.C. Clifton, J. Pizarro, J.A. Warner, D.K. Shuh, R.K. Strong, K.N. Raymond, The siderocalin/enterobactin interaction: a link between mammalian immunity and bacterial iron transport, J. Am. Chem. Soc. 130 (2008) 11524–11534.
[13] T.M. Hoette, R.J. Abergel, J. Xu, R.K. Strong, K.N. Raymond, The role of electrostatics in siderophore recognition by the immunoprotein siderocalin, J. Am. Chem. Soc. 130 (2008) 17584–17592.
[14] T.B. Karpishin, M.S. Gebhard, E.I. Solomon, K.N. Raymond, Spectroscopic studies of the electronic structure of iron(III) tris(catecholates), J. Am. Chem. Soc. 113 (1991) 2977–2984.
[15] C.M. Breneman, K.B. Wiberg, Determining atom-centered monopoles from molecular electrostatic potentials. The need for high sampling density in formamide conformational analysis, J. Comp. Chem. 11 (1990) 361–373.
[16] M.J. Frisch, G.W. Trucks, H.B. Schlegel, G.E. Scuseria, M.A. Robb, J.R. Cheeseman, G. Scalmani, V. Barone, B. Mennucci, G.A. Petersson, H. Nakatsuji, M. Caricato, X. Li, H.P. Hratchian, A.F. Izmaylov, J. Bloino, G. Zheng, J.L. Sonnenberg, M. Hada, M. Ehara, K. Toyota, R. Fukuda, J. Hasegawa, M. Ishida, T. Nakajima, Y. Honda, O. Kitao, H. Nakai, T. Vreven, J.A. Montgomery Jr., J.E. Peralta, F. Ogliaro, M. Bearpark, J.J. Heyd, E. Brothers, K.N. Kudin, V.N. Staroverov, R. Kobayashi, J. Normand, K. Raghavachari, A. Rendell, J.C. Burant, S.S. Iyengar, J. Tomasi, M. Cossi, N. Rega, J.M. Millam, M. Klene, J.E. Knox, J.B. Cross, V. Bakken, C. Adamo, J. Jaramillo, R. Gomperts, R.E. Stratmann, O. Yazyev, A.J. Austin, R. Cammi, C. Pomelli, J.W. Ochterski, R.L. Martin, K. Morokuma, V.G. Zakrzewski, G.A. Voth, P. Salvador, J.J. Dannenberg, S. Dapprich, A.D. Daniels, Ö. Farkas, J.B. Foresman, J.V. Ortiz, J. Cioslowski, D.J. Fox, Gaussian 09, Gaussian, Inc., Wallingford, CT, 2009.
[17] R.F.W. Bader, Atoms in Molecules: A Quantum Theory, Clarendon, Oxford, 1990.
[18] P. Popelier, Atoms in Molecules: An Introduction, Prentice-Hall, Harlow, 2000.
[19] F.W. Biegler-Konig, R.F.W. Bader, T.H. Hang, Calculation of the average properties of atoms in molecules. II, J. Comp. Chem. 3 (1982) 317–328.
[20] L.F. Pacios, A. Fernandez, CheckDen, a program to compute quantum molecular properties on spatial grids, J. Mol. Graphics Modell. 28 (2009) 102–112.
[21] The PyMOL Molecular Graphics System, Version 1.5.0.4 Schrödinger, LLC, 2013.
[22] N.A. Baker, D. Sept, S. Joseph, M.J. Holst, J.A. McCammon, Electrostatics of nanosystems: application to microtubules and the ribosome, Proc. Natl. Acad. Sci. USA 98 (2001) 10037–10041.
[23] J. Wang, P. Cieplak, P.A. Kollman, How well does a restrained electrostatic potential (RESP) model perform in calculating conformational energies of organic and biological molecules? J. Comp. Chem. 21 (2000) 1049–1074.
[24] T.J. Dolinsky, J.E. Nielsen, J.A. McCammon, N.A. Baker, Pdb2pqr: an automated pipeline for the setup of Poisson–Boltzmann electrostatics calculations, Nucleic Acids Res. 32 (2004) W665–W667.
[25] M.E. Davis, J.A. McCammon, Electrostatics in biomolecular structure and dynamics, Chem. Rev. 90 (1990) 509–521.
[26] O. Trott, A.J. Olson, AutoDock Vina, Improving the speed and accuracy of docking with a new scoring function, efficient optimization, and multithreading, J. Comp. Chem. 31 (2009) 455–461.
[27] G.M. Morris, R. Huey, W. Lindstrom, M.F. Sanner, R.K. Belew, D.S. Goddsell, A.J. Olson, Autodock4, AutoDockTools4: automated docking with selective receptor flexibility, J. Comp. Chem. 16 (2009) 2785–2791.
[28] L.F. Pacios, L. Tordesillas, A. Palacín, R. Sánchez-Monge, G. Salcedo, A. Díaz-Perales, LocaPep., Localization of epitopes on protein surfaces using peptides from phage display libraries, J. Chem. Inform. Model. 51 (2011) 1465–1473.
[29] L.F. Pacios, Arvomol/Contour. Molecular surface areas and volumes on personal computers, Comput. Chem. 18 (1994) 377–385.
[30] E. Krissinel, K. Henrick, Inference of macromolecular assemblies from crystalline state, J. Mol. Biol. 372 (2007) 774–797.
[31] E. Krissinel, Crystal contacts as nature's docking solutions, J. Comp. Chem. 31 (2010) 133–143.
[32] E. Krissinel, K. Henrick, Detection of protein assemblies in crystals, in: M.R. Berthold (Ed.), Computational Life Sciences, Lecture Notes in Computer Science, 3695, Springer-Verlag, Berlin, 2005, pp. 163–174.
[33] L.F. Pacios, L. Gómez, Conformational changes of the electrostatic potential of biphenyl: A theoretical study, Chem. Phys. Lett. 432 (2006) 414–420.
[34] L.F. Pacios, A theoretical study of the intramolecular interaction between proximal atoms in planar conformations of biphenyl and related systems, Struct. Chem. 18 (2007) 785–795.
[35] R.J. Cheng, P.Y. Chen, T. Lovell, T. Liu, L. Noodleman, D.A. Case, Symmetry and bonding in metalloporphyrins. A modern implementation for the bonding analyses of five- and six-coordinate high-spin iron(III)-porphyrin complexes through density functional theory calculations and NMR spectroscopy, J. Am. Chem. Soc. 125 (2003) 6774–6783.
[36] C.R. Bhattacharjee, P. Goswani, P. Mondal, Synthesis, structural characterization, and DFT studies of new mixed-ligand iron(III) Schiff-base complexes, J. Coord. Chem. 63 (2010) 2002–2011.
[37] W.M.I. Hassan, E.M. Zayed, A.K. Elkholy, H. Moustafa, G.G. Mohamed, Spectroscopic and density functional theory investigation of novel Schiff base complexes, Spectrosc. Acta A 103 (2013) 378–387.
[38] G. Brewer, C. Brewer, G. White, R.J. Butcher, C. Viragh, E.E. Carpenter, A. Schmiedekamp, Syntheses and characterization of iron(II) and iron(III) complexes of a tripodal ligand derived from tris(2-aminoethyl)methane, Inorg. Chim. Acta 362 (2009) 4158–4166.
[39] A.J. Simaan, M.L. Boillot, R. Carrasco, J. Cano, J.J. Girerd, T.A. Mattioli, J. Ensling, H. Spiering, P. Gutlich, Electronic, vibrational, and structural properties of a spin-crossover catecholato-iron system in the solid state: theoretical study of the electronic nature of the doublet and sextet states, Chem. Eur. J. 11 (2005) 1779–1793.
[40] B.F. Matzanke, Iron transport: siderophores, in: R.B. King (Ed.), Encyclopedia of Inorganic Chemistry, IV, second ed., Wiley, New York, 2005, pp. 2619–2646.
[41] S. Suresh, V.C. Srivastava, I.M. Mishra, Adsorption of catechol, resorcinol, hydroquinone, and their derivatives: a review, Int. J. Energy Environ. Eng. 3 (2012) 32–50.
[42] O. Gálvez, P.C. Gómez, L.F. Pacios, Variation with the imtermolecular distance of properties dependent on the electron density in hydrogen-bond dimers, J. Chem. Phys. 115 (2001) 11166–11184.
[43] O. Gálvez, P.C. Gómez, L.F. Pacios, Variation with the imtermolecular distance of properties dependent on the electron density in cyclic dimers with two hydrogen-bonds, J. Chem. Phys. 118 (2003) 4878–4895.
[44] L.F. Pacios, Topological descriptors of the electron density and the electron localization function in hydrogen bond dimers at short intermonomer distances, J. Phys. Chem. A 108 (2004) 1177–1188.
[45] L.F. Pacios, P.C. Gómez, Dependence of calculated NMR proton chemical shifts on electron density in proton transfer processes on short strong hydrogen-bonds, J. Phys. Chem. A 108 (2004) 11783–11792.
[46] L.F. Pacios, O. Gálvez, P.C. Gómez, Variation of geometries and electron properties along proton transfer in strong hydrogen-bond complexes, J. Chem. Phys. 122 (2005), 214307-1-11.
[47] W.D. Arnold, E. Oldfield, The chemical nature of hydrogen bonding in proteins via NMR: J-couplings, chemical shifts, and AIM theory, J. Am. Chem. Soc. 122 (2000) 12835–12841.
[48] H.J. Woo, Calculation of absolute protein–ligand binding constants with the molecular dynamics free energy perturbation method, in: A. Kukol (Ed.), Molecular Modeling of Proteins, Humana Press, Totowa, NJ, USA, 2010, pp. 109–120.
[49] V. Zoete, M.A. Cuendet, A. Grosdidier, O. Michielin, SwissParam, a fast force field generation tool for small organic molecules, J. Comput. Chem. 32 (2011) 2359–2368.